NDT&E International 156 (2025) 103481

Contents lists available at ScienceDirect

NDT and E International

journal homepage: www.elsevier.com/locate/ndteint

Research Paper

U-NET autoencoder for amplitude recovery on binarized Full Matrix Captures

Aurélien Thon [a,*], Guillaume Painchaud-April [b], Alain Le Duff [b], Pierre Bélanger [a]

[a] PULÉTS, École de Technologie Supérieure (ÉTS), 1100 R. Notre Dame O, Montreal, H3C 1K3, Quebec, Canada
[b] Evident Scientific, 3415 Rue Pierre-Ardouin, Quebec, G1P 0B3, Quebec, Canada

ARTICLE INFO

Keywords:
Nondestructive testing
Ultrasound
Phased array
Neural network
UNET autoencoder
Binary signals
Amplitude recovery

ABSTRACT

Full Matrix Capture (FMC) and the Total Focusing Method (TFM) are instrumental techniques in ultrasonic nondestructive testing (NDT) in industries such as aerospace, oil and gas, and manufacturing, and allow efficient defect detection by capturing all possible transmitter–receiver pairs and generating highly resolved images on a predefined pixel grid. The use of dense linear or matrix probes presents significant challenges in data storage and transfer but also in the complexity of the acquisition system's electronics. In this context, binary acquisition steps in as an attractive alternative for simplifying acquisition equipment and reducing data size. However, binary formats carry the drawback of amplitude information loss. To address this, the present study explores the application of a U-NET autoencoder neural network to reconstruct amplitude data from binarized FMC signals. The autoencoder's U-NET architecture is particularly suited for this task due to its effectiveness with limited datasets, a common issue in NDT. Finite element simulations were used to generate training and validation datasets. Experimental tests were then conducted on steel samples containing various defects, such as Electrical Discharge Machining (EDM) cracks, side-drilled holes (SDH), and a realistic fatigue crack in a steel bar. The reconstructed FMC data were evaluated using TFM images and Structural Similarity Index Measure (SSIM), showing that the neural network accurately reconstructed FMCs. Notwithstanding the presence of minor amplitude errors, the spatial positioning of defects remained precise, demonstrating the method's viability for practical NDT applications.

1. Introduction

The Full Matrix Capture (FMC) and the Total Focusing Method (TFM) represent significant advancements in ultrasonic nondestructive testing (NDT) [1–3]. They greatly improve defect detection across industries such as aerospace, oil and gas, and manufacturing. FMC involves the acquisition of signals from all possible transmitter–receiver pairs, enabling TFM to generate images by focusing these signals on a predefined pixel grid. These methods enhance defect detection, including cracks, inclusions, and delaminations [4–7]. They can be further improved with advanced techniques such as multimode imaging for defects at varying orientations [8,9] or phase coherence imaging (PCI) for small, highly diffractive geometries [10–13].

The growing complexity of data management and electronics for dense or matrix probes underscores the need for innovative data acquisition and compression techniques. Several approaches have been explored to reduce data size without compromising imaging quality. One method is to lower the sampling frequency, but this approach is constrained by the Nyquist–Shannon theorem. Compressive sensing allows sub-Nyquist sampling frequency for sparse signals, which is the case for Ascans [14,15]. Another method involves reducing the number of firing events, leveraging the high redundancy of information present in an FMC to reduce the number of active elements during transmission, enabling faster acquisition with a very minimal impact on TFM image quality.[16–18]. A third option, compressing the amplitude axis of A-scans, is particularly promising.

Binary signal acquisition offers substantial advantages in data reduction and instrumentation cost, making it a compelling alternative to traditional methods. Unlike approaches such as compressive sensing or sparse array acquisition, binary acquisition not only reduces data size but also simplifies hardware requirements by replacing analog-to-digital converters with comparators. However, its primary drawback lies in the deterioration of TFM image quality. Binary FMC data lack the destructive interferences essential for conventional TFM, leading to poor quality images. Additionally, the interpretation of A-scans becomes more challenging, as amplitude information is removed. Nevertheless, certain characteristics remain detectable in binary A-scans: noise manifests as rapid and random variations between 0 and 1, while an echo will oscillate at the frequency of the generated signal.

Neural networks (NN) have proven to be effective tools for numerous areas of ultrasonic testing, including (1) signal deconvolution [19],

* Corresponding author.
E-mail address: aurelien.thon@pulets.ca (A. Thon).

https://doi.org/10.1016/j.ndteint.2025.103481
Received 20 March 2025; Received in revised form 9 June 2025; Accepted 30 June 2025
Available online 12 July 2025

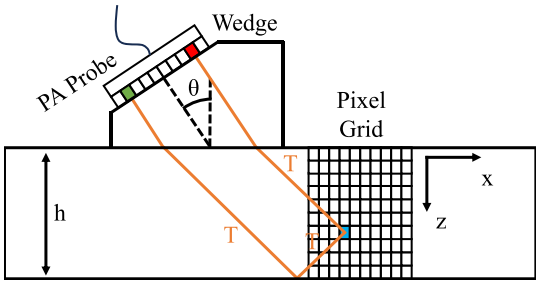

Fig. 1. Explanatory diagram of the Total Focusing Method (TFM) imaging principle.

(2) classification [20], (3) detection [21], (4) segmentation [22], and (5) image generation [23]. One of the main weaknesses of using NN in nondestructive testing (NDT) is the small size of the databases available for training. Unlike databases in sectors such as medical or image recognition, those in the NDT field are limited by the number of experimental acquisitions, simulations and data sharing. In 2015, a group of researchers developed a particularly high-performance autoencoder structure for limited databases namely the U-NET architecture [24].

Although binary acquisition instruments are still in development and not yet commercially available, progress is being made. The aim of the present work is to use a U-NET autoencoder network to reconstruct the amplitude from signals that has already been binarized. This method will lay the groundwork for deploying binary acquisition systems in the field, enabling users to visualize individual A-scans as if they were captured with a conventional instrument. The quality of this reconstruction is assessed by performing TFM imaging from the standard FMC and the one reconstructed by the NN. These images will then be compared with the structural similarity index measure (SSIM).

This article is divided as follows: Section 2 presents all the necessary scientific background required for the study such as FMC acquisition, TFM imaging, the U-NET autoencoder architecture, an introduction to the Structural Similarity Index Measure (SSIM) and a description of the training, validation and experimental testing datasets. Section 3 present the simulated and experimental results, followed by a discussion about the proposed method in Section 4. Finally, a conclusion is drawn.

2. Materials and method

2.1. Full matrix capture and total focusing method

Ultrasonic imaging is an essential tool in NDT, providing advanced capabilities for material inspection without causing damage. Among the most significant developments in this area are the FMC and TFM [1,2]. FMC involves the acquisition of a comprehensive dataset by capturing all possible transmit–receive combinations from an array of elements, thereby providing a dense and highly detailed ultrasonic data matrix. An FMC can be assimilated into a matrix in three dimensions: (1) a temporal axis, (2) the transmitting elements and (3) the receiving elements. The first dimension is determined by the number of time increments acquired and the sampling frequency, while dimensions (2) and (3) depend on the number of elements (N) in the probe, resulting in a total size of N^2. This measurement protocol therefore produces large quantities of data, all the more so for high-frequency acquisitions and dense probes, such as 128-elements or matrix probes which can easily contain a few thousand elements.

This rich dataset is then processed using the TFM, an advanced beamforming technique that focuses the wave on a predefined pixel grid. If a pixel grid described in Fig. 1 is considered, the TFM can be calculated at each pixel position (x,z) with the following equation:

$$I_{\mathrm{TFM}}(x,z) = \left| \sum_{k=1}^{N} \sum_{l=1}^{N} \tilde{y}_{kl}\left(\tau_{kl}(x,z)\right) \right| \tag{1}$$

where $\tilde{y}_{kl}(t)$ is the analytic signal at a given time $\tau_{kl}(x,z)$ which corresponds to the time-of-flight between the emitter k to the pixel, and back to the receiver l. When using a wedge, multiple ray paths can be considered. As most phased array probes are longitudinally polarized, the wave path in the wedge is generally omitted in the nomenclature. T stands for a transverse mode and L for a longitudinal mode. For example, the TT-T path means that there is a skip before the defect with a reflection from the back wall using the transverse mode, and a T direct path from the defect to the front wall.

Several studies have shown that the amount of data recorded during an FMC acquisition can be drastically reduced with little effect on the quality of the images produced. Time axis compression is conventionally limited by the Nyquist–Shannon theorem, but techniques such as compressive sensing can reduce the sampling rate to a fraction of this limit when considering a sparse signal which is the case for Ascans in ultrasonic testing [15]. Considering the high redundancy of information in an FMC, a reduction of the spatial dimensions with sparse array acquisition [16–18] can also be considered. However, the amplitude of the signal in this case could still be affected. This magnitude is recorded digitally, and is generally coded between 12 and 16 signed bits. By definition, maximum compression means reducing the amplitude to a binary value. Phase imaging techniques such as Phase Coherence Imaging (PCI) [10,11,25] can still be used, as the phase of the signal can be recovered from a binary signal. However, the absence of destructive interference when applying conventional TFM produces images of poor quality.

2.2. U-Net autoencoder

An autoencoder (AE) [26,27] is a type of artificial neural network that uses an unlabeled database. The architecture consists of two parts: (1) an encoder which reduces the dimensionality of the data to extract its most important features into a latent space, and (2) a decoder which uses the latent space to reconstruct the input data. Once trained, these networks can be used to generate data similar to those in the original dataset. Employing low-noise or noiseless data for loss calculation, also allows using AEs for image or signal denoising [28,29].

The U-Net architecture is a specific case of convolutional autoencoders, and derives its name from its symmetrical U-shaped structure. Originally developed for biomedical image segmentation [24,30], it is now also used for image denoising [31,32] and upscaling [33]. The encoder generally consists of repeated convolutional and max-pooling allowing the extraction of important features in the latent space. These features are then up-sampled by a corresponding decoder. Unlike other AEs, the encoder's features in this case are saved and then concatenated to the corresponding decoder layer through connecting path. This notably allows the NN to better carry to context of the input data along the different layers of the structure, thus increasing the accuracy of the reconstructed data. This architecture has been shown to perform very well for small databases, which is particularly interesting in the case of NDT.

The model used in the present study is very similar to the original version proposed by Ronneberge et al. [24,30], and was built using the Pytorch library. The encoder is also composed of successive applications of two 3×3 convolutions, each followed by a batch normalization layer ($\varepsilon = 1e^{-5}$) and a ReLU activation function. Downsampling is done with a 2×2 max pooling operation with stride 2. Each step in the decoder starts with an upsampling with a 2×2 transposed convolution. A concatenation is made with the corresponding feature map from the encoder. Then, multiple double 3×3 convolutions each followed by a batch normalization layer ($\varepsilon = 1e^{-5}$) and a ReLU activation, are applied. For the final layer a 1×1 convolution layer is applied. For each stage of the encoder, the number of convolutional filters is indicated in Fig. 2 and follows the sequence 64, 128, 256, and 512; the decoder mirrors this structure with 512, 256, 128, and 64 filters, respectively. One of the differences between Ronneberge et al.'s model and that used in this

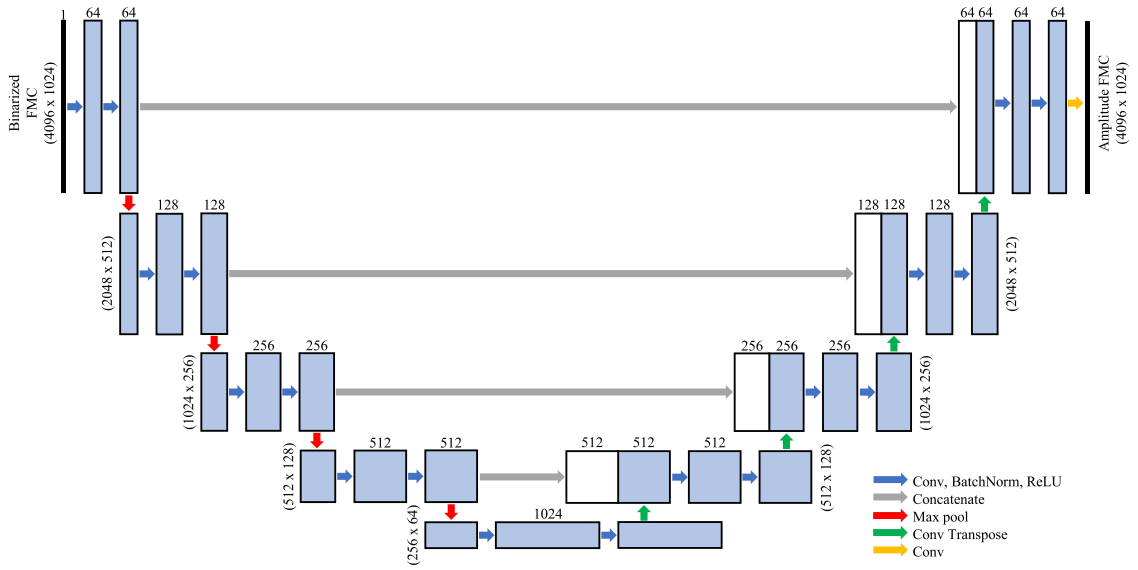

Fig. 2. Autoencoder U-Net model used.

paper is that here, padding is added at each convolution layer to avoid losing any border pixel and to remove the cropping required in the original version.

The input consists of a full binarized FMC, where all A-scans are provided at once as a 4096 (number of samples) by 1024 (32-element probe) matrix. Here the number of elements was limited to 32 to meet graphics memory requirements during network training. An Adam optimizer was used with PyTorch's default parameters ($\beta_1 = 0.9$, $\beta_2 = 0.999$, $\varepsilon = 1e^{-8}$). The output was compared to the corresponding standard non-binary FMC with a Mean Square Error (MSE) loss function. The learning rate was selected through a manual search, retaining the value that resulted in the lowest validation loss while minimizing overfitting, as indicated by the smallest divergence between the training and validation loss curves. A value of 2×10^{-4} was ultimately chosen. The batch size was constrained to a value of 1 due to computational resource limitations. The number of epoch was controlled with an early stopping routine which ended the training when the validation loss stopped improving for 100 epochs. Whenever this happened, the NN weights were set to the configuration value at which the validation loss was minimal.

2.3. Structural similarity index measure

In order to judge the network's ability to reconstruct the FMC from binary data, it was decided to use a TFM algorithm with both the base and the reconstructed FMCs. These two images were compared with the SSIM. This metric was developed in 2004 [34], and is used to compare an image with another reference image. It is usually calculated on windows f and g of these two images using the following equation:

$$\mathrm{SSIM}(f,g) = \frac{\left(2\mu_f\mu_g + c_1\right)\left(2\sigma_{fg} + c_2\right)}{\left(\mu_f^2 + \mu_g^2 + c_1\right)\left(\sigma_f^2 + \sigma_g^2 + c_2\right)} \tag{2}$$

where μ_f and μ_g are the mean value of the windows f and g, σ_f^2 and σ_g^2 the variance in the windows f and g, σ_{fg} is the covariance of f and g. c_1 and c_2 are two constants used to stabilize the function when the denominator is close to 0. In general, $c_1 = \left(k_1 L\right)^2$ and $c_2 = \left(k_2 L\right)^2$ with $k_1 = 0.01$ and $k_2 = 0.03$, and L is the dynamic range of the pixel values. In our case the values of the TFM images were normalized between 0 and 1 so $L = 1$. Once all these local SSIMs are calculated, a global SSIM can be obtained by applying an average to these local values. The more identical the two images compared, the closer the SSIM value will be to 1. On the contrary, for two images with large differences, this value will tend towards 0.

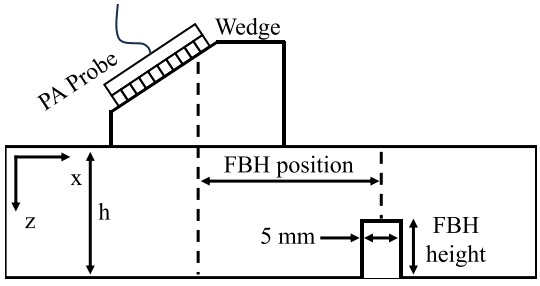

Fig. 3. Diagram of the developed finite element models.

2.4. Training and validation

The data used for training and validation were generated solely using finite element simulations. This choice was motivated by the simplicity of constructing the database, both with respect to the inspected block and the position and size of a defect. The simulations were performed on Pogo FEA [35], a GPU-accelerated solver.

In each case, the model consisted of a 25 mm homogeneous and isotropic steel plate, with a density of $\rho = 8000$ kg/m^3, a Young modulus of E = 210 GPa and a Poisson ratio of $\nu = 0.30$ modeled in 2D. The emission system consisted of an Evident 5L64-32X10-A32-P-2.5-OM probe associated with the Evident SA32-N55S-IHC wedge, with only the first 32 elements being modeled to limit the size of the FMC. A flat-bottom hole (FBH) with a diameter of 5 mm, with its position varying from 25 to 75 mm in front of the probe's center line (5 increments), and whose depth varied from a quarter to half of the plate's thickness (4 increments), was present on the backwall of the plate, for a total of 20 models (Fig. 3). Absorbing boundaries [36] were added at the ends of the plate (x-axis) to reduce the model size by minimizing edge echoes.

The excitation signal used was a 5-cycle Hann-windowed toneburst centered at 5 MHz. The length of the excitation signal was similar to the time response of the elements of the 5L64-32X10-A32-P-2.5-OM probe when excited by a half-cycle burst produced by most industrial inspection equipment. The element size was defined to ensure at least 25 elements per the shortest wavelength, and to guarantee result convergence, the time step was chosen such that a mode could not skip an element within a time increment.

Table 1
Experimental and simulation parameters.

Probe		
	Model	5L64-32X10-A32-P-2.5-OM
	Central frequency	5 MHz
	Active elements (total)	32 (64)
	Pitch	0.5 mm
Wedge		
	Model	SA32-N55S-IHC
	Angle	36.1°
	Material	Rexolite
	Longitudinal velocity	2330 m/s
Specimens		
	Material	Steel
	Longitudinal velocity	5940 m/s
	Shear velocity	3243 m/s

The obtained FMCs were then resampled at a sampling frequency of 50 MHz and reorganized to have dimensions of 4096 × 1024 (32-elements FMC). The initial burst was nullified as it is an unusable section of the matrix. To approximate the signal that could be obtained experimentally, filtered white noise within the probe's bandwidth was added. The FMCs were then binarized by associating a positive value with a high state and a null or negative value with a low state. The binary FMCs were used as input for the neural network, while the standard FMCs were used for loss calculation.

2.5. Testing

The testing dataset was built using only experimental data. A Verasonics Vantage 64 LE was used for the acquisition system, and the same probe and wedge as the ones modeled were used. The A-scans were acquired on Matlab in signed 16-bit integers, with value ranging from −32,768 to +32,767, and then binarized with the routine described in the previous section. Although a purely binary acquisition system would have been preferable to demonstrate the capabilities of such a network, a standard FMC is nonetheless required to quantify the performance of the trained network.

Three samples were used for the experimental acquisitions (see Fig. 4). The first two blocks were 19 mm steel plates. The first block contained EDM cracks with a width of 0.3 mm, extending vertically by 5 mm, but with inclinations of 90°, 80°, 70°, and 60° relative to the backwall. The second block contained several groups of two side drilled holes (SDH) created by EDM, with a diameter of 0.3 mm, also spaced vertically by 5 mm, and centered in the thickness. The axis connecting these SDHs was inclined at 90°, 80°, 70°, and 60° relative to the bottom of the piece. These specimens were chosen to test the NN's ability to reconstruct an FMC when the wave interacts with defects whose position, dimension, orientation, and nature differ from those included in the simulated training dataset.

The last sample was a 24.54 mm thick steel bar, including a fatigue crack of 8.6 mm. In this case, the objective was to test the method's performance on realistic defects.

The experimental and simulation parameters are summarized in Table 1.

3. Results

3.1. Training solely on simulated data

The network (Fig. 2) was trained on a server with two NVIDIA QUADRO P6000 GPUs. This process was completed in 1267 epochs, according to the following strategy: early stopping whenever the validation loss stopped improving for more than 100 epoch. All weights were then restored to the configuration that allowed for minimal validation loss, which was 9.17×10^{-4} at epoch 1167 (Fig. 5). This stage was completed in 8.5 h and used approximately 23 GB of VRAM.

Examples of reconstructions using the training dataset are presented in Fig. 6. Fig. 6(a) shows an FMC obtained by simulation, and Fig. 6(b) shows its binarized version. Fig. 6(c) is the version reconstructed by the UNET network. At first glance, the differences between the original and reconstructed FMCs are barely noticeable. The different modes and echoes appear to be present in both cases at the same locations. To compare these two matrices more precisely, the Ascan obtained when the first element emits and the 16th element receives is displayed in Fig. 6(d). To facilitate visibility, the time axis was zoomed in around a section including 2 relatively close echoes and noises. The original and reconstructed versions are presented in blue and red, in a standard and binary format respectively. The binary signal in black represents the absolute error between the two binary signals. Several observations can be made from Fig. 6(d). Firstly, there is no phase shift between the original Ascan and its reconstructed version. Secondly, the echoes oscillate around the same frequency and have the same length. The primary difference visible in the standard signals is an error in amplitude; a slight discrepancy is visible between the two versions of the Ascan. This error is not constant, and appears to be smaller for the second echo than for the first one. When examining the binary signals, one can observe more errors between the simulated and reconstructed signals, which are easily visible on the black curve. However, these errors are all located in regions of low amplitude. Near the echoes, no errors are present in the binary signals.

To evaluate whether these errors will impact a potential inspection, TFM images were calculated around the defect. These are shown in Fig. 7. Fig. 7(a) corresponds to the TFM image obtained using a T-T wave path with the FMC from the simulations, and Fig. 7(b) uses the reconstructed FMC. Here again, few differences are visible to the naked eye. A metric such as SSIM (Fig. 7(c)) reveals that the main errors (low SSIM values) are located at the edges of the indications, regardless of whether they are defects or artifacts. As for the larger indications, the center is reconstructed with high fidelity (SSIM value close to 1). This is consistent with the observations made in Fig. 6(d) since the absence of errors on the time axis (phase shift or delay) does not cause positioning errors, while an error in the shape and therefore the amplitude of the echoes will result in a modification of the shape of the indications. Notwithstanding the observed errors, these two images remain very similar, making it difficult to determine which of the two was created using simulated data and which was generated by the neural network.

3.2. Experimental verification

Experimental tests were conducted to evaluate the method's generalization capabilities across various configurations, including different block thicknesses and various defect characteristics (size, orientation, nature, and number).

The first inspected plate is the one with four increasingly inclined open EDM notches at 90°, 80°, 70° and 60° relative to the bottom of the piece. The results are presented in Fig. 8. The first row, Fig. 8(a) to (d), shows the TFM images obtained with the experimental measurements; Fig. 8(e) to (h) shows the images obtained using the data reconstructed by the network, and Fig. 8(i) to (l) show the SSIM figures. The cases are organized by column: Fig. 8(a), (e), and (i) are obtained using the measurements on the vertical crack at 90° ; (b), (f), and (j) on the crack at 80° ; and so on. To better visualize the inclination of the crack between the different cases, the wave path used for reconstruction varies as a function of the configuration: the TT-T path is used for the cracks at 90° and 80°, and the TT-TT path for those at 70° and 60° . The same observations as in the previous section can be made, namely that the errors are mostly present at the edges of the indications. A noteworthy particularity on the vertical crack is that the quantity or intensity of artifacts seems lower when using the reconstructed data as compared to the experimental data.

Fig. 4. Different steel samples with defects used during experimental verification.

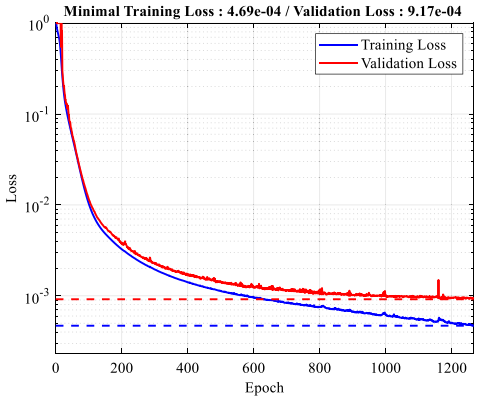

Fig. 5. Evolution of the loss on the training and validation datasets during network training with a learning rate of 2×10^{-4}.

The second plate used includes four groups of two SDHs. Fig. 8 shows the various TFM and SSIM images. The organization of the subfigures is the same as in Fig. 9. One difference in this case is that the TT-TT path is used for all the images. The same observations as before can be made. The original TFM and the one obtained using the reconstructed FMCs show indications in the same locations in both cases, with an error at the edges of the indications visible thanks to the SSIM, but indiscernible directly on the TFM images.

3.3. Realistic defect

The final experimental measurements were conducted on a 24.54 mm thick steel bar incorporating a fatigue crack occupying 35% (length of 8.6 mm). This allowed for testing on realistic defects with more irregular profiles as compared to EDM-machined notches or SDH (see Fig. 10).

In this case, it can be noted that the fatigue crack is clearly visible in both TFM images. These reconstructions are very similar to those obtained with a perfectly machined notch and less so to a fatigue crack. This can be explained by the fact that the frequency used is 5 MHz; an increase in frequency would improve the resolution. The limitation of the active probe elements to 32 also reduces the image precision. However, if we consider only the quality of the TFM image (Fig. 9(b)) obtained using the FMC reconstructed by the network, the same observations as previously can be made, namely, there is an error in amplitude at the edges of the indications but no positioning error. It is also interesting to note that the reconstructed image (Fig. 9(b)) seems to present fewer artifacts than the original one (Fig. 9(a)).

4. Discussion

The last section demonstrated the performance of the UNET network in reconstructing an FMC from binary data, which is much lighter to store, using TFM images, a standard in ultrasonic NDT. The training database is quite limited, containing only 20 simulated FMCs (15 for training and 5 for validation), with only FBHs being modeled. However, the results showed similar performances in each investigated case for different configurations, whether in terms of thickness, nature, position, or number of defects. A possible reason for these generalization capabilities is that the network's objective is not to reconstruct a TFM image, but rather to directly reconstruct the Ascans that compose the FMC. In this sense, the training database consists of 20,480 Ascans.

The main error noted is an alteration in the echo shape, which induces errors in the TFM images, at the edges of the indications rather than on their positions. These discrepancies are barely visible in the TFM images and are only highlighted by the SSIM. This effect would therefore only have a small impact on the sizing and positioning of a defect. Several reasons can explain this phenomenon. The simulations were performed on steel plates without attenuation. The only considered amplitude loss is the spreading of the ultrasonic beam. Therefore, the network has learned to reconstruct the FMC with minimal attenuation and may overestimate the amplitude of the echoes, especially as the propagation duration increases. Taking attenuation into account during the simulations could reduce this problem, but this would only be valid for an inspection on a given material. Additionally, this effect can also be present without using the network developed for this project. Indeed, the shape of an echo in ultrasonic inspection is mainly influenced by the central frequency and the bandwidth of a piezoelectric element. These two parameters can vary between two theoretically identical elements, and even within the same phased array probe.

The next improvements to the model will address several current limitations. First, the number of active elements is currently limited to 32, due to the high VRAM requirements during training. Optimizing the network architecture, such as reducing the number or size of layers, will be necessary to support a higher number of elements. Second, the probe frequency was fixed in order to limit the duration of the simulations used to generate the training dataset, which are already time-consuming, particularly when a wedge is modeled. While varying

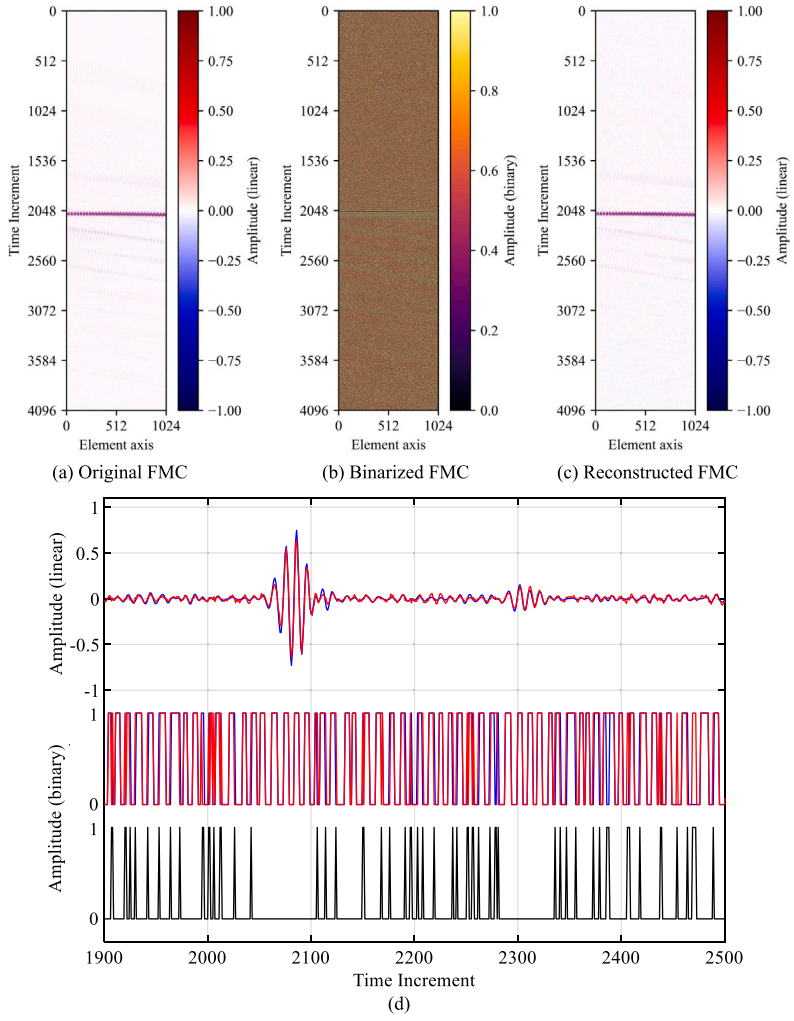

Fig. 6. Example of FMC included in the training dataset: (a), (b), and (c) correspond to the FMC from the simulations, the binary version of this FMC, and the one reconstructed by the UNET network, respectively. (d) corresponds to an example of an Ascan from these FMCs, zoomed in on two echoes, including the original signal (blue) and the reconstructed signal (red) as well as their binary versions in the corresponding colors and the absolute error between the reconstructed and original binary signal (black).

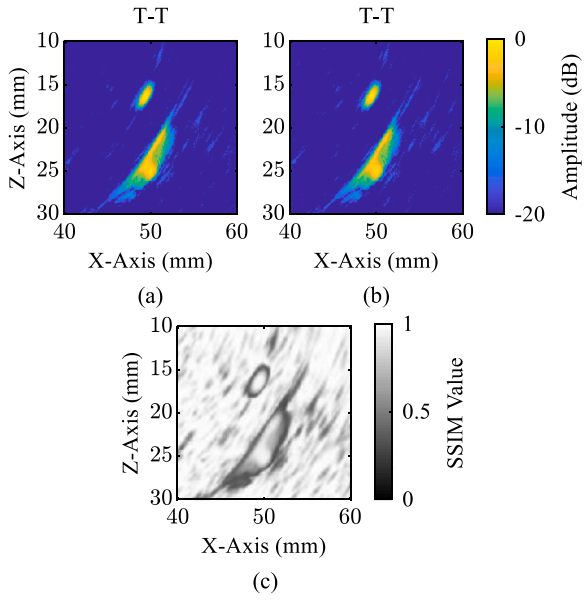

Fig. 7. TFM images obtained using the original FMC (a) and reconstructed FMC (b) presented in Fig. 6, along with the SSIM (c).

the frequency in future simulations could enhance the model's generality, this would significantly increase the size and generation time of the dataset. In addition, an important next step will be to extend the model's capabilities to inspect a wider range of materials. Currently, the model produces significant artifacts and reconstruction errors when the acoustic velocity of the inspected material deviates substantially from that of steel, the material used for training. Overcoming this limitation will require incorporating a more diverse set of materials into the training dataset to improve the model's robustness and ability to generalize across different inspection conditions.

A binary acquisition system is currently under development. It is expected to reduce FMC storage requirements by a factor of 16, assuming a 16-bit signed digitization similar to that used by the Verasonics system. By considering only the FMC and no other contextual information, recording one of the experimental FMCs in binary format reduces the file size from 8192 KB to 512 KB. This gain will be even more interesting for acquisitions with denser probes (e.g., 64–128 elements or matrix probes) or over a longer duration. Subsequently, the proposed technique will allow for the retrieval of an FMC and Ascans compatible with classical TFM and signal that are easier to interpret visually.

The reconstruction delay was evaluated under different hardware configurations. It ranges from approximately 30 s on a standard laptop without GPU acceleration to about 1 s on a server equipped with two Nvidia Quadro P6000 GPUs, the same system used for training the

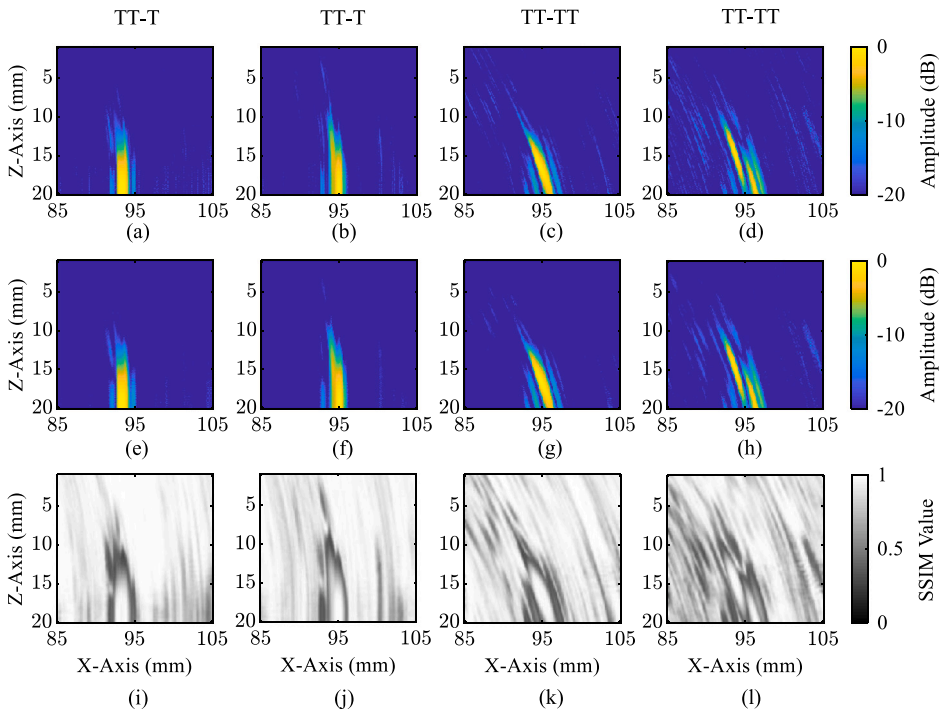

Fig. 8. TFM images obtained with experimental acquisitions on samples containing open cracks (a), (b), (c), and (d), and from data reconstructed by the U-NET network (e), (f), (g), and (h), as well as the corresponding SSIM (i), (j), (k), and (l). The cracks are inclined at 90° (a-e-i), 80° (b-f-j), 70° (c-g-k) and 60° (d-h-l) relative to the sample backwall.

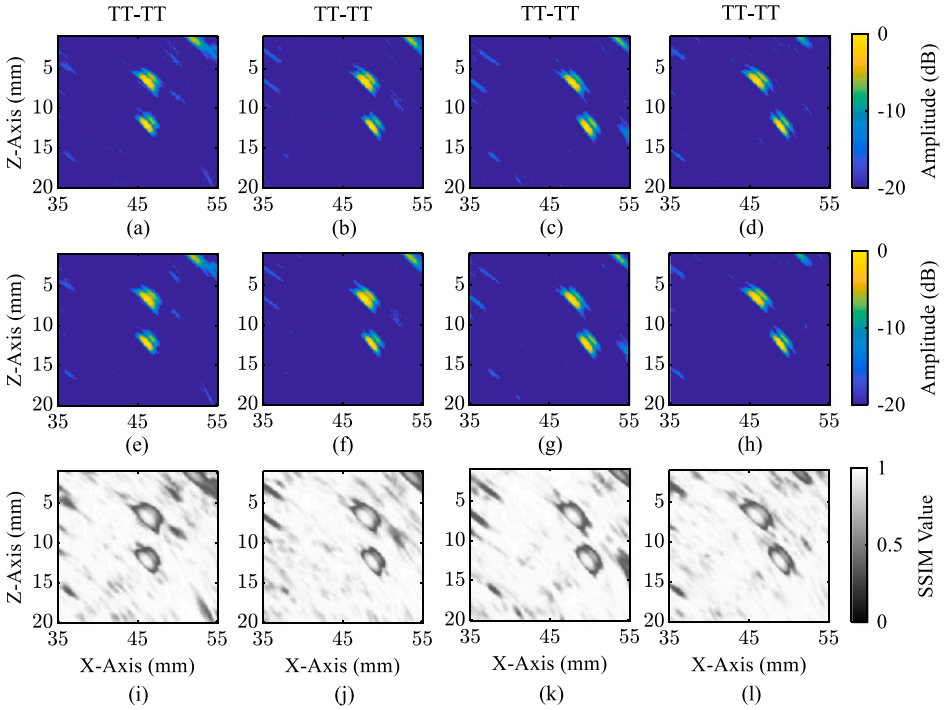

Fig. 9. TFM images obtained with experimental acquisitions on samples containing four groups of two SDHs each (a), (b), (c), and (d), and from data reconstructed by the U-NET network (e), (f), (g), and (h), as well as the corresponding SSIM (i), (j), (k), and (l). The axes connecting the SDHs are inclined at 90° (a-e-i), 80° (b-f-j), 70° (c-g-k) and 60° (d-h-l) relative to the bottom of the sample.

network. This additional processing time currently limits the applicability of the method for real-time inspections, as most industrial devices are not designed for AI-based processing. However, in many on-site inspection scenarios, it is not necessarily required to access the full amplitude data immediately. Providing the user with views such as PCI (which can be computed directly from binary data) is often sufficient. If amplitude data is eventually required during the inspection, a practical solution would be to either transfer the compressed binary FMC over the internet to a remote computation server, or store it locally and perform the reconstruction later on more powerful equipment. This approach provides greater flexibility in managing computational resources and adapting to operational constraints.

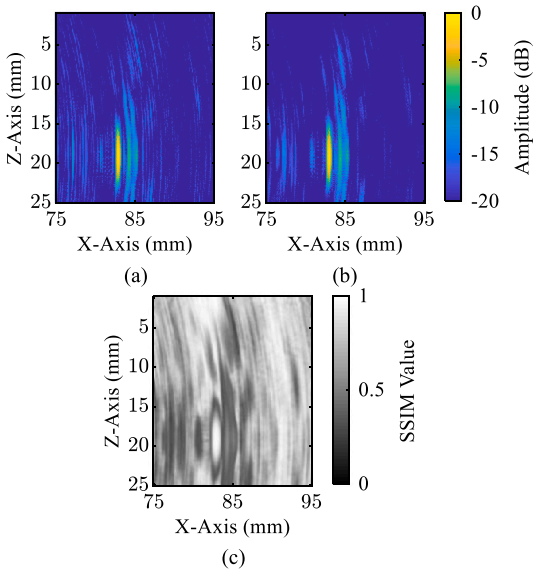

Fig. 10. TFM images obtained from an experimental FMC (a) acquired on a block containing a fatigue crack occupying 35% of the thickness, or 8.6 mm in height, from the FMC reconstructed by the U-NET network (b), and the corresponding SSIM (c).

5. Conclusion

In this study, a UNET model was used to recover the amplitude of a binarized signal. The training data was generated exclusively through finite element simulations, allowing for easy generation and great control of parameters such as the specimen thickness, and the nature, dimension, and size of defects. The capabilities of the UNET network were verified using various experimental measurements, including notches and EDM machined SDHs, as well as a block containing a fatigue crack. TFM images were used to compare the experimental FMCs with those reconstructed by the neural network, as TFM is a standard imaging method in ultrasonic NDT. The images showed a faithful reconstruction of the indications, and without metrics such as SSIM or an individual examination of the Ascans, detecting error is a complex or even impossible proposition. The main errors observed were in the amplitude and shape of the echoes and at the edges of the indications on the TFM images, but no errors were observed in the temporal position of the echoes or at the phase of the signal. The observed errors will have only a minimal effect on the positioning and sizing of the defects.

The proposed method confirms the feasibility of a binary acquisition system, offering a simplified and cheaper electronic design and significantly reducing data size. Importantly, it achieves these benefits without compromising data interpretation or the performance of advanced algorithms like the Total Focusing Method (TFM).

CRediT authorship contribution statement

Aurélien Thon: Writing – review & editing, Writing – original draft, Validation, Software, Methodology, Investigation, Data curation, Conceptualization. **Guillaume Painchaud-April:** Writing – review & editing, Conceptualization. **Alain Le Duff:** Writing – review & editing, Conceptualization. **Pierre Bélanger:** Supervision, Project administration, Methodology, Funding acquisition, Conceptualization, Writing – review & editing, Validation.

Declaration of competing interest

The authors declare that they have no known competing financial interests or personal relationships that could have appeared to influence the work reported in this paper.

Acknowledgments

This research was funded by Natural Sciences and Engineering Research Council of Canada (NSERC) grant number ALLRP 576710-22, Mitacs, Canada and the Olympus Industrial Research Chair on Ultrasonic Nondestructive Testing.

Data availability

Data will be made available on request.

References

[1] Holmes C, Drinkwater BW, Wilcox PD. Post-processing of the full matrix of ultrasonic transmit–receive array data for non-destructive evaluation. NDT E Int 2005;38(8):701–11. http://dx.doi.org/10.1016/j.ndteint.2005.04.002, URL https://www.sciencedirect.com/science/article/pii/S0963869505000721.

[2] Drinkwater BW, Wilcox PD. Ultrasonic arrays for non-destructive evaluation: A review. NDT E Int 2006;39(7):525–41. http://dx.doi.org/10.1016/j.ndteint.2006.03.006, URL https://www.sciencedirect.com/science/article/pii/S0963869506000272.

[3] Schmerr LW. Fundamentals of ultrasonic phased arrays. Solid mechanics and its applications, vol. 215, Cham: Springer International Publishing; 2015, http://dx.doi.org/10.1007/978-3-319-07272-2, URL https://link.springer.com/10.1007/978-3-319-07272-2.

[4] Lin L, Cao H, Luo Z. Total focusing method imaging of multidirectional CFRP laminate with model-based time delay correction. NDT E Int 2018;97:51–8. http://dx.doi.org/10.1016/j.ndteint.2018.03.011, URL https://www.sciencedirect.com/science/article/pii/S0963869517305546.

[5] Javadi Y, Macleod CN, Pierce SG, Gachagan A, Kerr W, Ding J, Williams S, Vasilev M, Su R, Mineo C, Dziewierz J. Ultrasonic phased array inspection of wire + arc additive manufacture samples using conventional and total focusing method imaging approaches. Insight - Non- Destr Test Cond Monit 2019;61(3):144–8. http://dx.doi.org/10.1784/insi.2019.61.3.144.

[6] Han X-l, Wu W-t, Li P, Lin J. Application of ultrasonic phased array total focusing method in weld inspection using an inclined wedge. In: Proceedings of the 2014 symposium on piezoelectricity, acoustic waves, and device applications. 2014, p. 114–7. http://dx.doi.org/10.1109/SPAWDA.2014.6998539, URL https://ieeexplore.ieee.org/abstract/document/6998539.

[7] Pillarisetti LSS, Anandamurugan S. Ultrasonic inspection of weld defects using total focusing method. In: Mukhopadhyay CK, Mulaveesala R, editors. Advances in non-destructive evaluation. Singapore: Springer; 2021, p. 187–202. http://dx.doi.org/10.1007/978-981-16-0186-6_19.

[8] Zhang J, Drinkwater BW, Wilcox PD, Hunter AJ. Defect detection using ultrasonic arrays: The multi-mode total focusing method. NDT E Int 2010;43(2):123–33. http://dx.doi.org/10.1016/j.ndteint.2009.10.001, URL https://www.sciencedirect.com/science/article/pii/S0963869509001480.

[9] Felice MV, Velichko A, Wilcox PD, Lane CJL. Depth measurement of small surface-breaking cracks using the half-skip total focusing method. AIP Conf Proc 2015;1650(1):994–1000. http://dx.doi.org/10.1063/1.4914706.

[10] Camacho J, Parrilla M, Fritsch C. Phase coherence imaging. 2009, URL https://ieeexplore.ieee.org/document/4976281.

[11] Camacho J, Atehortua D, Cruza JF, Brizuela J, Ealo J. Ultrasonic crack evaluation by phase coherence processing and TFM and its application to online monitoring in fatigue tests. NDT E Int 2018;93:164–74. http://dx.doi.org/10.1016/j.ndteint.2017.10.007, URL https://www.sciencedirect.com/science/article/pii/S0963869516303073.

[12] Dupont-Marillia F, Krynicki JW, Bélanger P. Early detection of high temperature hydrogen attack using the ultrasonic full matrix capture and advanced post-processing methods. NDT E Int 2022;130:102676. http://dx.doi.org/10.1016/j.ndteint.2022.102676, URL https://www.sciencedirect.com/science/article/pii/S0963869522000755.

[13] Gauthier B, Painchaud-April G, Le Duff A, Bélanger P. Towards an alternative to time of flight diffraction using instantaneous phase coherence imaging for characterization of crack-like defects. Sensors 2021;21(3):730. http://dx.doi.org/10.3390/s21030730, URL https://www.mdpi.com/1424-8220/21/3/730, Number: 3 Publisher: Multidisciplinary Digital Publishing Institute.

[14] Candes E, Romberg J, Tao T. Robust uncertainty principles: exact signal reconstruction from highly incomplete frequency information. IEEE Trans Inform Theory 2006;52(2):489–509. http://dx.doi.org/10.1109/TIT.2005.862083, URL https://ieeexplore.ieee.org/abstract/document/1580791, Conference Name: IEEE Transactions on Information Theory.

[15] Piedade LP, Painchaud-April G, Le Duff A, Bélanger P. Compressive sensing strategy on sparse array to accelerate ultrasonic TFM imaging. IEEE Trans Ultrason Ferroelectr Freq Control 2023;70(6):538–50. http://dx.doi.org/10.1109/TUFFC.2023.3266719, URL https://ieeexplore.ieee.org/abstract/document/10100889, Conference Name: IEEE Transactions on Ultrasonics, Ferroelectrics, and Frequency Control.

[16] Piedade LP, Painchaud-April G, Le Duff A, Bélanger P. Minimum transmission events for fast ultrasonic TFM imaging: A comparative study. NDT E Int 2022;128:102627. http://dx.doi.org/10.1016/j.ndteint.2022.102627, URL https://www.sciencedirect.com/science/article/pii/S0963869522000263.

[17] T. Schiefler N, M. Maia J, K. Schneider F, J. Zimbico A, A. Assef A, T. Costa E. Generation and analysis of ultrasound images using plane wave and sparse arrays techniques. Sensors 2018;18(11):3660. http://dx.doi.org/10.3390/s18113660, URL https://www.mdpi.com/1424-8220/18/11/3660, Number: 11 Publisher: Multidisciplinary Digital Publishing Institute.

[18] Hu H, Du J, Ye C, Li X. Ultrasonic phased array sparse-TFM imaging based on sparse array optimization and new edge-directed interpolation. Sensors 2018;18(6):1830. http://dx.doi.org/10.3390/s18061830, URL https://www.mdpi.com/1424-8220/18/6/1830, Number: 6 Publisher: Multidisciplinary Digital Publishing Institute.

[19] Chapon A, Pereira D, Toews M, Belanger P. Deconvolution of ultrasonic signals using a convolutional neural network. Ultrasonics 2021;111:106312. http://dx.doi.org/10.1016/j.ultras.2020.106312, URL https://www.sciencedirect.com/science/article/pii/S0041624X2030247X.

[20] Munir N, Kim H-J, Park J, Song S-J, Kang S-S. Convolutional neural network for ultrasonic weldment flaw classification in noisy conditions. Ultrasonics 2019;94:74–81. http://dx.doi.org/10.1016/j.ultras.2018.12.001, URL https://www.sciencedirect.com/science/article/pii/S0041624X18305754.

[21] Virupakshappa K, Marino M, Oruklu E. A multi-resolution convolutional neural network architecture for ultrasonic flaw detection. In: 2018 IEEE international ultrasonics symposium (IUS). 2018, p. 1–4. http://dx.doi.org/10.1109/ULTSYM.2018.8579888, URL https://ieeexplore.ieee.org/document/8579888.

[22] Nair AA, Tran TD, Reiter A, Lediju Bell MA. A deep learning based alternative to beamforming ultrasound images. In: 2018 IEEE international conference on acoustics, speech and signal processing (ICASSP). 2018, p. 3359–63. http://dx.doi.org/10.1109/ICASSP.2018.8461575, URL https://ieeexplore.ieee.org/document/8461575.

[23] Molinier N, Painchaud-April G, Le Duff A, Toews M, Bélanger P. Ultrasonic imaging using conditional generative adversarial networks. Ultrasonics 2023;133:107015. http://dx.doi.org/10.1016/j.ultras.2023.107015, URL https://www.sciencedirect.com/science/article/pii/S0041624X23000914.

[24] Ronneberger O, Fischer P, Brox T. U-Net: Convolutional networks for biomedical image segmentation. In: Navab N, Hornegger J, Wells WM, Frangi AF, editors. Medical image computing and computer-assisted intervention – MICCAI 2015. Cham: Springer International Publishing; 2015, p. 234–41. http://dx.doi.org/10.1007/978-3-319-24574-4_28.

[25] Gauthier B, Painchaud-April G, Le Duff A, Belanger P. Lightweight and amplitude-free ultrasonic imaging using single-bit digitization and instantaneous phase coherence. IEEE Trans Ultrason Ferroelectr Freq Control 2022;69(5):1763–74. http://dx.doi.org/10.1109/TUFFC.2022.3163621, URL https://ieeexplore.ieee.org/document/9745038, Conference Name: IEEE Transactions on Ultrasonics, Ferroelectrics, and Frequency Control.

[26] Hinton GE, Salakhutdinov RR. Reducing the dimensionality of data with neural networks. Science 2006;313(5786):504–7. http://dx.doi.org/10.1126/science.1127647, URL https://www.science.org/doi/abs/10.1126/science.1127647, Publisher: American Association for the Advancement of Science.

[27] Kingma DP, Welling M. Auto-encoding variational Bayes. 2022, http://dx.doi.org/10.48550/arXiv.1312.6114, URL http://arxiv.org/abs/1312.6114, arXiv:1312.6114 [cs, stat].

[28] lu X, Tsao Y, Matsuda S, Hori C. Speech enhancement based on deep denoising auto-encoder. 2013, Pages: 440.

[29] Gondara L. Medical image denoising using convolutional denoising autoencoders. In: 2016 IEEE 16th international conference on data mining workshops (ICDMW). 2016, p. 241–6. http://dx.doi.org/10.1109/ICDMW.2016.0041, URL https://ieeexplore.ieee.org/abstract/document/7836672.

[30] Çiçek Ö, Abdulkadir A, Lienkamp SS, Brox T, Ronneberger O. 3D U-net: Learning dense volumetric segmentation from sparse annotation. In: Ourselin S, Joskowicz L, Sabuncu MR, Unal G, Wells W, editors. Medical image computing and computer-assisted intervention – MICCAI 2016. Cham: Springer International Publishing; 2016, p. 424–32. http://dx.doi.org/10.1007/978-3-319-46723-8_49.

[31] Zhang K, Zuo W, Chen Y, Meng D, Zhang L. Beyond a Gaussian denoiser: Residual learning of deep CNN for image denoising. IEEE Trans Image Process 2017;26(7):3142–55. http://dx.doi.org/10.1109/TIP.2017.2662206, URL https://ieeexplore.ieee.org/abstract/document/7839189, Conference Name: IEEE Transactions on Image Processing.

[32] Gurrola-Ramos J, Dalmau O, Alarcón TE. A residual dense U-Net neural network for image denoising. IEEE Access 2021;9:31742–54. http://dx.doi.org/10.1109/ACCESS.2021.3061062, URL https://ieeexplore.ieee.org/abstract/document/9360532, Conference Name: IEEE Access.

[33] Ledig C, Theis L, Huszar F, Caballero J, Cunningham A, Acosta A, Aitken A, Tejani A, Totz J, Wang Z, Shi W. Photo-realistic single image super-resolution using a generative adversarial network. 2017, http://dx.doi.org/10.48550/arXiv.1609.04802, URL http://arxiv.org/abs/1609.04802, arXiv:1609.04802 [cs, stat].

[34] Wang Z, Bovik A, Sheikh H, Simoncelli E. Image quality assessment: from error visibility to structural similarity. IEEE Trans Image Process 2004;13(4):600–12. http://dx.doi.org/10.1109/TIP.2003.819861, URL https://ieeexplore.ieee.org/abstract/document/1284395, Conference Name: IEEE Transactions on Image Processing.

[35] Huthwaite P. Accelerated finite element elastodynamic simulations using the GPU. J Comput Phys 2014;257:687–707. http://dx.doi.org/10.1016/j.jcp.2013.10.017, URL http://www.sciencedirect.com/science/article/pii/S0021999113006931.

[36] Drozdz M, Moreau L, Castaings M, Lowe MJS, Cawley P. Efficient numerical modelling of absorbing regions for boundaries of guided waves problems. AIP Conf Proc 2006;820(1):126–33. http://dx.doi.org/10.1063/1.2184520, URL https://aip.scitation.org/doi/abs/10.1063/1.2184520.